Ionospheric Plasma Depletions at Mars Observed by the MAVEN spacecraft

Praveen Basuvaraj[1], Frantisek Nemec[2], Zdenek Nemecek[1], and Jana Safrankova[1]

[1]Charles University, Faculty of Mathematics and Physics
[2]Charles University

November 23, 2022

Abstract

The Martian ionosphere, modulated by the solar wind from the topside and remnant crustal magnetic fields close to the surface, possesses unique structures different from Earth and Venus. Integrated observations by the plasma and magnetic field instruments onboard the Mars Atmosphere and Volatile Evolution (MAVEN) spacecraft show evidence of ionospheric plasma depletions, independent of seasonal variations at Mars. During such depletions, the density of all ionospheric ion species is reduced by more than an order of magnitude, and, at the same time, the electron temperature increases abruptly. An automated algorithm for the identification of such plasma depletions is developed. Altogether, as many as 1177 events are identified in 8618 orbits available from October 2014 to May 2021. A statistical investigation of these events reveals that they are more prominent on the nightside. Their higher occurrence in the southern hemisphere suggests a possible relation to the crustal magnetic fields. While the dayside events occur mainly at altitudes above about 200 km, nightside event altitudes are typically lower. Considering the relation between spacecraft velocity and observed event duration, we suggest that the depletions are bubble-like structures, more elongated horizontally than vertically. A possible mechanism of their formation is discussed.

Ionospheric Plasma Depletions at Mars Observed by the MAVEN spacecraft

Praveen Basuvaraj, František Němec, Zdeněk Němeček, Jana Šafránková

[1]Charles University, Faculty of Mathematics and Physics, Prague, Czech Republic

Key Points:

- Density depletions larger than an order of magnitude are observed for all major ionospheric ion species and electrons.
- The depletions are more prominent on the nightside, mainly in the southern hemisphere, suggesting a relation to crustal magnetic fields.
- While most dayside depletions occur at altitudes above 200 km, their altitudes on the nightside are typically below 250 km.

Corresponding author: Praveen Basuvaraj, `praveen.basuvaraj@matfyz.cuni.cz`

Abstract

The Martian ionosphere, modulated by the solar wind from the topside and remnant crustal magnetic fields close to the surface, possesses unique structures different from Earth and Venus. Integrated observations by the plasma and magnetic field instruments onboard the Mars Atmosphere and Volatile Evolution (MAVEN) spacecraft show evidence of ionospheric plasma depletions, independent of seasonal variations at Mars. During such depletions, the density of all ionospheric ion species is reduced by more than an order of magnitude, and, at the same time, the electron temperature increases abruptly. An automated algorithm for the identification of such plasma depletions is developed. Altogether, as many as 1177 events are identified in 8618 orbits available from October 2014 to May 2021. A statistical investigation of these events reveals that they are more prominent on the nightside. Their higher occurrence in the southern hemisphere suggests a possible relation to the crustal magnetic fields. While the dayside events occur mainly at altitudes above about 200 km, nightside event altitudes are typically lower. Considering the relation between spacecraft velocity and observed event duration, we suggest that the depletions are bubble-like structures, more elongated horizontally than vertically. A possible mechanism of their formation is discussed.

Plain Language Summary

Ions and electrons embedded in an atmosphere of a planet constitute the ionospheric plasma. At Mars, the ionospheric plasma has a well-defined altitude structure similar to Earth. However, we find that the normally smooth plasma density profiles exhibit at times significant sudden plasma depletions. We use nearly 7 years of data obtained by the Mars Atmosphere and Volatile Evolution (MAVEN) spacecraft to systematically analyze the occurrence and properties of such events. We show that, during the events, the density of all monitored ion species decreases at least ten times and, at the same time, the temperature increases. The events are more frequent and occur at lower altitudes on the nightside than on the dayside. We show that the event geometry corresponds to bubble-like structures rather than to layers and/or columns of decreased density. We discuss several possible mechanisms of their formation.

1 Introduction

Mars is an unmagnetized planet with a thin layer of atmosphere compared to Earth. Due to the precipitation of energetic solar charged particles (mostly electrons) and the absorption of incoming solar radiation (EUV and X-rays), the neutral atmosphere of Mars gets ionized to form the dayside ionosphere composed of ions and free electrons (Krasnopolsky, 2002; Němec et al., 2010). The dayside ionosphere is photochemically controlled below the exobase (about 220 km) (Mendillo et al., 2017). On the other hand, the nightside ionosphere is formed - apart from the impact ionization by precipitating energetic particles - due to the plasma transport from the dayside (Fox et al., 1993; Lillis et al., 2009; Lillis & Fang, 2015).

First in-situ observations of the Martian neutral atmosphere and charged ionosphere were performed by the Viking Landers 1 and 2 through their Neutral Mass Spectrometer (NMS) and Retarding Potential Analyzer (RPA) instruments (Owen & Biemann, 1976; Soffen, 1976; McElroy et al., 1976). Nier and McElroy (1976) used the NMS data to demonstrate that CO_2 is the dominant neutral atmospheric species representing about 95% of the total atmosphere of Mars with few traces of N_2, Ar, and O. The RPA data revealed that the Martian ionosphere is populated by O_2^+ ion followed by CO_2^+, O^+, and NO^+ (Hanson et al., 1977). Under a photochemical equilibrium of the dayside ionosphere, the average peak ionization altitude is about 125 km with a peak electron density of about $1.5\times10^5\,\mathrm{cm}^{-3}$ (e.g., Withers, 2009; Němec, Morgan, Gurnett, Duru, & Truhlík, 2011; Andrews, Andersson, et al., 2015, and references therein).

The structure and composition of the ionosphere are highly variable due to the coupling with the neutral atmosphere and plasma environment (Bougher, Cravens, et al., 2015; Bougher, Pawlowski, et al., 2015). The absence of a magnetic field allows for a direct interaction of the ionosphere with the solar wind plasma, thereby influencing the ionospheric dynamics (Acuña et al., 1998; Mitchell et al., 2001). The localized remnant crustal magnetic sources dispersed over the Martian crust are insignificant in balancing the solar wind dynamic pressure on the dayside. Still, they considerably affect the formation of the nightside ionosphere. They may, in particular, inhibit the plasma transport from the dayside (Němec et al., 2010) and control the regions where energetic particles precipitate and form localized ionization patches (Němec, Morgan, Gurnett, & Brain, 2011; Lillis et al., 2011; Girazian et al., 2017). Ionospheric ion and electron densities are related to the solar activity, solar zenith angle, precipitating energetic particle fluxes, and neutral abundances (Withers et al., 2012; Lillis et al., 2015; Sánchez-Cano et al., 2016). In addition, orbit-to-orbit ionospheric variability, as well as the variability of altitude-density profiles within individual orbits, have been reported (Duru et al., 2008; Bougher, Jakosky, et al., 2015).

Mitchell et al. (2001) noticed suprathermal electron flux depressions in the Mars Global Surveyor (MGS) Electron Reflectometer data, which represent sudden drops in the fluxes by at least two orders of magnitude, and they introduced the term “plasma voids” for such depletions. These voids are seen within the nightside closed crustal magnetic field lines at altitudes below 200 km (Xu et al., 2017). The Mars Advanced Radar for Subsurface and Ionospheric Sounding (MARSIS) instrument (Picardi et al., 2005) on board the Mars Express spacecraft has revealed the existence of electron depressions in the nightside ionosphere (Duru et al., 2011). However, the spacecraft orbit spatially constrained this study to altitudes above 275 km. The average width of electron depressions estimated from 66 full orbits is found to be 950 km.

Withers et al. (2012) utilized the electron density profiles, retrieved from the Mars Express Radio Science Experiment (MaRS), to reveal peculiar features present at times in the upper ionosphere, indicating major departures from conditions in models that produce a Chapman layer-like shape. Depressions in the suprathermal electrons that vary with altitude and solar illumination conditions were studied using Mars Express, MGS, and MAVEN probes (Steckiewicz et al., 2015; Hall et al., 2016; Steckiewicz et al., 2017). Collinson et al. (2020) reported the existence of sporadic E-like structures (layers and rifts) in the Martian dayside ionosphere, contributing to the sudden increase or depletion of plasma density within the atmospheric dynamo region (all layers and rifts were encountered below 223 km). It was suggested that they are, analogically to the situation at Earth, formed in the dynamo region; the ions are dragged by neutral winds across the magnetic field lines, resulting in electromagnetic forces and eventually, depending on the configuration, in the layer/rift formation.

In the present study, we use nearly 7 years (about 3.5 Martian years) of MAVEN spacecraft measurements to systematically check for the presence of ionospheric plasma depletions and to analyze their occurrence and properties as a function of relevant parameters. The used data set is described in section 2. An automated method used for the event identification is described in section 3. The results obtained are presented in section 4 and discussed in section 5. Finally, section 6 contains a brief summary of the main findings.

2 Data Set

The Mars Atmosphere and Volatile Evolution (MAVEN) probe reached Mars on 21 September 2014. Its primary objectives are to estimate the atmospheric loss rate, to determine the composition of neutral and ionized constituents, and to reveal the major parameters controlling their loss through time (Lillis et al., 2015; Jakosky et al., 2015).

The MAVEN spacecraft orbits Mars along an elliptical orbit with a nominal periapsis of about 150 km to sample the upper atmospheric region and its orbital period is about 4.5 h. With an orbital inclination of 75°, the spacecraft observations can provide a quasi-global coverage of Mars (Jakosky et al., 2015). We utilized the plasma and magnetic measurements in the Martian ionosphere from three onboard instruments.

The Neutral Gas and Ion Mass Spectrometer (NGIMS) instrument is a quadrupole mass spectrometer that samples the atmospheric neutrals and ions in the mass range of 2-150 Da (Mahaffy, Benna, King, et al., 2015). NGIMS operates at altitudes below 500 km. Each inbound/outbound orbital part of the NGIMS measurements lasts for about 600 s with a vertical resolution of about 5 km for targeted species (Bougher, Jakosky, et al., 2015; Mahaffy, Benna, Elrod, et al., 2015). In our study, we use the NGIMS data from 18 October 2014 to 14 May 2021, comprising of 8618 orbits in total. Number densities of the major ionospheric constituents O^+, O_2^+, NO^+, and CO_2^+ are used.

The Langmuir Probe and Waves (LPW) instrument consists of two identical 40 cm probe sensors mounted on a pair of about 7 m long booms (Andersson et al., 2015). These sensors are used to measure current-voltage characteristics that are, in turn, used to calculate the electron density and temperature of the local plasma environment. The time resolution of the measurements is 4 s and the sensitivity of the instrument is 10^2–10^6 cm^{-3} for the electron density and 500–50000 K (*i.e.,* ≈0.04 to 4.3 eV) for the temperature. We use the electron density (N_{e^-}) and electron temperature (T_{e^-}) measurements in concurrence with the ion density measurements by NGIMS.

The Magnetometer (MAG) instrument comprises of twin three-axial flux-gate magnetometers mounted at the tip of the spacecraft solar panels. The MAG instrument provides vector measurements of the magnetic field along the spacecraft trajectory at an intrinsic sampling rate of 32 vector samples per second (Connerney et al., 2015). The dual magnetometers were designed to operate at a dynamic range of about 60,000 nT with resolution up to 0.05 nT. The calibrated vector magnetic field measurements in the planetocentric coordinate system with a time resolution of 4 s are used in our study.

3 Identification of Plasma Depletion Events

An example of a plasma depletion event (PDE) is shown in Figure 1. Altitudinal profiles of ion densities (O^+, O_2^+, NO^+, CO_2^+) measured by the NGIMS instrument during the MAVEN outbound orbit #7003 on 06 May 2018 are shown by the color curves. Additionally, the electron density and temperature profiles measured by the LPW instrument are indicated by the black and red curves, respectively. The plasma depletion event is seen at altitudes between about 304 and 367 km, with the peak depletion roughly in the middle of the interval (336 km altitude). The start, peak, and stop altitudes of the event are marked by horizontal dashed lines and labeled z_{start}, z_{peak}, and z_{stop}, respectively.

At altitudes around z_{peak}, number densities of all analyzed ionospheric ion species are by more than an order of magnitude lower than at altitudes below/above. Similar depletion is also observed in electron densities. This may be expected, as the ionospheric plasma is quasi-neutral. However, given that the ion and electron densities are measured by two independent instruments, this represents a nice confirmation that the effect is indeed real and not instrumental. Additionally, the electron temperature is found to increase considerably during the event.

Showing an example PDE event and demonstrating its principal characteristics, we aim to systematically identify such events in the MAVEN data. The events are typically visually well identifiable in individual orbital plots similar to that in Figure 1, and their list might be thus, in principle, prepared manually. However, we develop an auto-

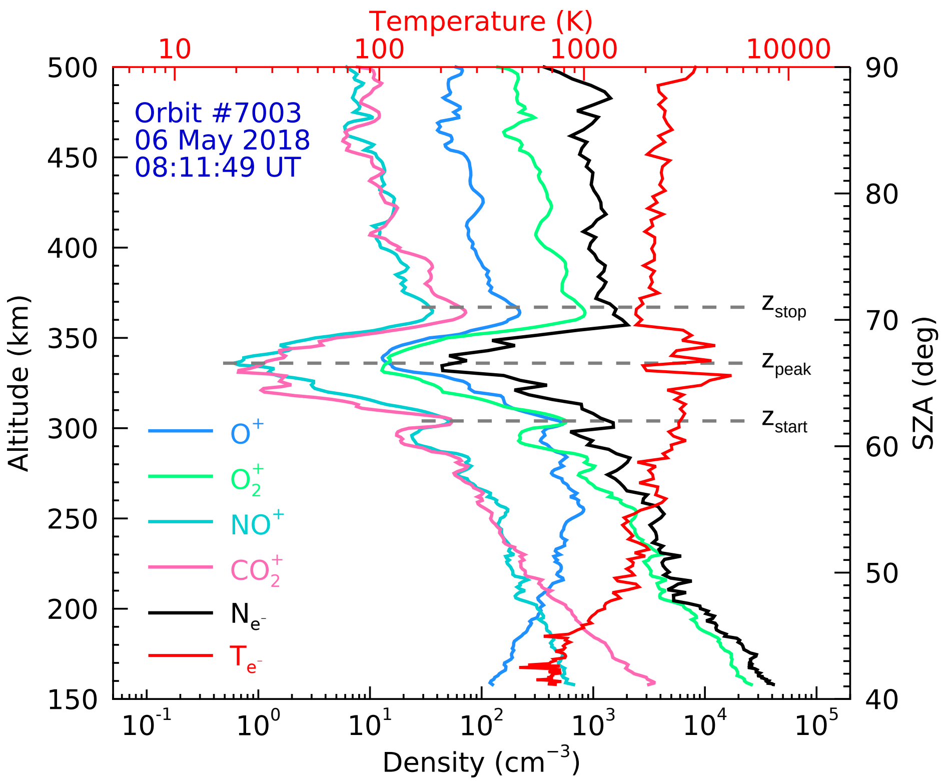

Figure 1. Ionospheric altitude profiles observed by the NGIMS and LPW instruments during orbit #7003 (outbound) on 06 May 2018. Plasma number densities of individual ion species and electron density are shown by the color and black curves, respectively. The altitudinal profile of the electron temperature is shown by the red curve using the scale at the top. A plasma depletion event, exhibiting a clear sudden decrease of plasma densities and an increase of the electron temperature, is seen at altitudes between about 304 km (z_{start}) and 367 km (z_{stop}). The peak depletion is observed at an altitude of about 336 km (z_{peak}).

matic identification routine, which has the advantage of exact quantitative criteria and, at the same time, it determines the values z_{start}, z_{peak}, and z_{stop}.

The procedure uses NGIMS measured density profiles of all major ionospheric ions (O^+, O_2^+, NO^+, CO_2^+). It assumes that the altitude range of PDE (depletion width hereafter) is between 5 and 80 km, which safely encompasses the width ranges of manually pre-identified events used for the routine development.

An identified PDE is required to have an average (over the four major ion species) peak density depletion larger than 90%:

$$\frac{1}{2N}\sum_{i=1}^{N}\left[\frac{n_i(z_{peak})}{n_i(z_{start})}+\frac{n_i(z_{peak})}{n_i(z_{stop})}\right]\leq 0.1 \tag{1}$$

where $n_i(z)$ is the number density of the ionospheric ion i at an altitude z and N is the total number of ionospheric ion species analyzed. In our case, N=4 corresponds to O^+, O_2^+, NO^+, and CO_2^+ ions.

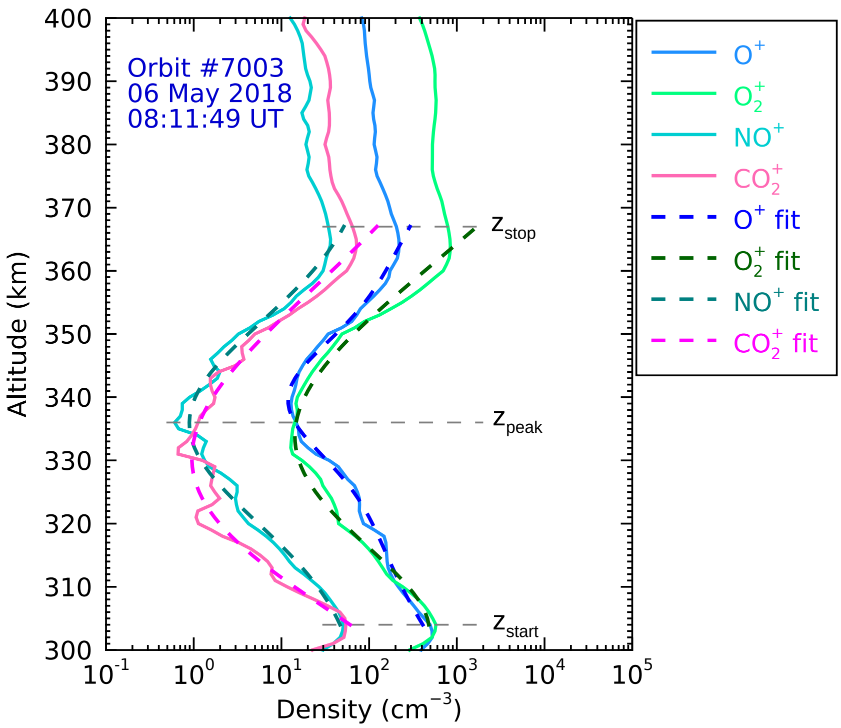

Figure 2. A zoomed view of ion density profiles from Figure 1, highlighting the depletion event as observed by the NGIMS instrument, is shown by the solid curves. The altitudes z_{start}, z_{peak}, and z_{stop} are identified using an automatic routine (see text). Gaussian fits of individual ion density profiles in between these altitudes are shown by the dashed curves.

Altitudes of NGIMS measurements range from the periapsis up to about 500 km, where the ionopause is periodically encountered (Benna et al., 2015). Considering this altitude limitation, we apply the aforementioned PDE identification criteria to the data measured at altitudes between 150 and 500 km during all the analyzed 8618 orbits. For each identified event, the altitudes z_{start}, z_{peak}, and z_{stop} are determined.

Figure 2 depicts a zoomed view of Figure 1, focusing on altitudes around the PDE and demonstrating the performance of the developed identification routine. We notice that the shapes of individual ion density profiles are similar over the depletion region, regardless of the actual ion abundances. Gaussian fits of ion density profiles in the altitude range between z_{start} and z_{stop} are over-plotted by dashed curves. The fits are based on the logarithm of ion densities rather than on the densities themselves. They include a linear background term to account for the gradual density decrease with the altitude. This allows us to define (separately for each ion density profile) a density ratio corresponding to the maximum plasma depletion as $r_N = n_{obs}/n_{est}$, where n_{obs} corresponds to the peak of the Gaussian fit and n_{est} corresponds to the respective linear term.

We note that up to three distinct PDEs are identified at different altitudes in some orbits. These are considered as separate events hereinafter. Altogether, as many as 1177 PDEs events are identified in 1060 half (inbound/outbound) orbits.

4 Results

4.1 Locations of Plasma Depletion Events

Figure 3 shows the locations of the detected PDEs over the Martian surface. The loci of PDEs depicted in the figure correspond to the altitude of peak depletions (z_{peak}). The events observed during the day and night are plotted by yellow stars and red circles, respectively. Model crustal magnetic field magnitude at an altitude of 400 km based on the Cain et al. (2003) magnetic field model is color-coded using the scale at the top. The remnant crustal fields are typically larger in the southern hemisphere than in the northern hemisphere, but there is no apparent relation to the event locations.

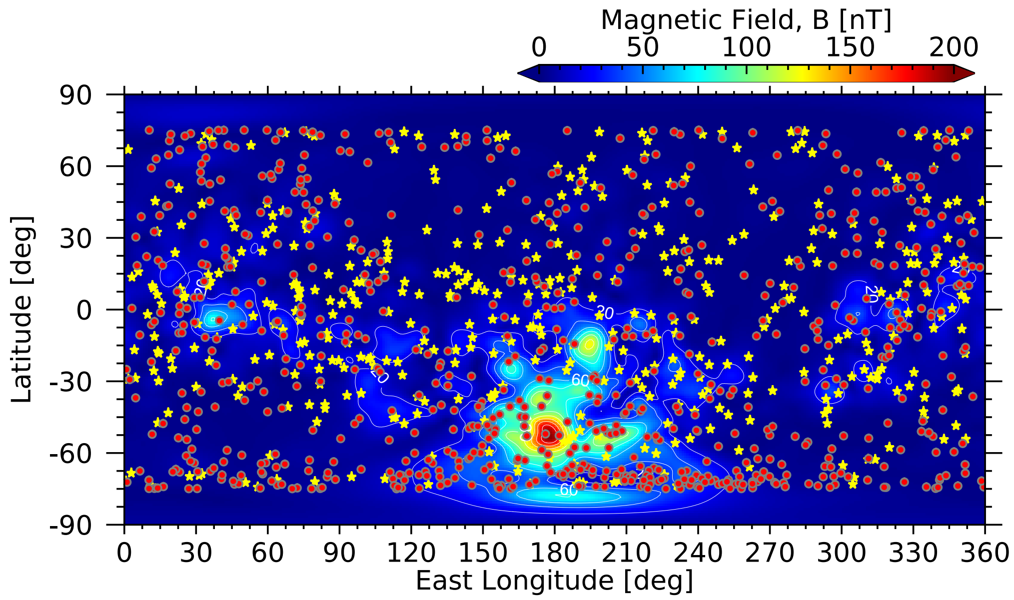

Figure 3. Locations of identified plasma depletion events. The daytime and nighttime events are shown as yellow stars and red circles, respectively. Model crustal magnetic field magnitude at 400 km (Cain et al., 2003) is color-coded using the scale at the top.

The total number of events and corresponding normalized occurrence rates (*i.e.,* number of events per hour of measurement) in the northern and southern hemispheres are given in Table 1. It can be seen that the events are more frequently observed on the nightside than on the dayside. Additionally, while the event occurrence is roughly the same in the northern and southern hemispheres during the day, the nighttime occurrence rate is significantly higher in the southern hemisphere.

The normalized occurrence rate (*i.e.,* number of events per hour of measurement) of PDEs is investigated as a function of possible controlling parameters in Figure 4. The occurrence rates as a function of local solar time (LST) and solar zenith angle (SZA) are investigated in Figures 4a and 4c, respectively. It can be seen that the probability of observing a depletion event during the nighttime is about 2–3 times higher than during the daytime, in agreement with the results in Table 1. The normalized event occurrence rate as a function of the altitude is depicted in Figure 4b. Although the events occur all over the analyzed altitudinal range, their occurrence seems to be somewhat lower at low ($<$ 170 km) and high ($>$ 450 km) altitudes. The dependence of the event occurrence rate

Table 1. Occurrence of plasma depletion events in northern/summer hemispheres

Parameter	Dayside A(B)	Nightside A(B)
Northern Hemisphere	205 (0.31)	275 (0.52)
Southern Hemisphere	224 (0.26)	473 (0.91)

A–number of events; B–normalized occurrence rate (h^{-1})

on the solar longitude shown in Figure 4d does not reveal any clear trend, demonstrating that the events occur relatively equally throughout all the seasons.

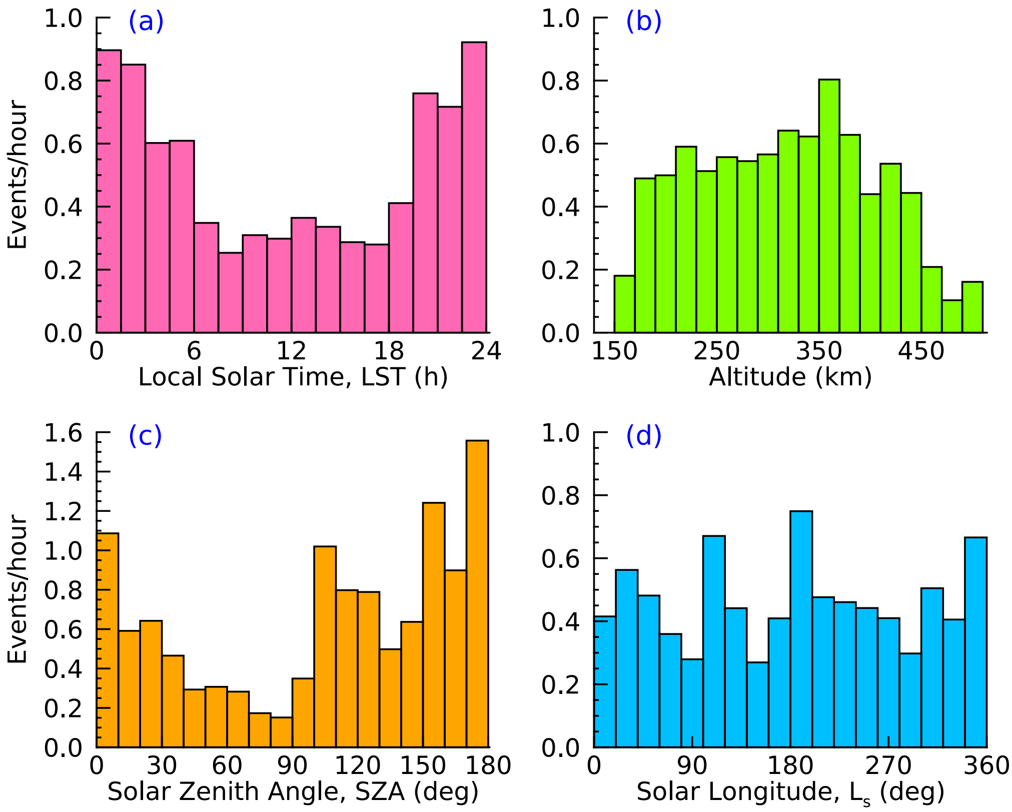

Figure 4. Normalized occurrence rates (number of events per hour) as a function of: (a) local solar time (LST), (b) altitude, (c) solar zenith angle (SZA), and (d) solar longitude (L_s).

Histograms of basic parameters of PDEs are shown in Figure 5. The altitudinal range of plasma depletion events (σ_Z) is analyzed in Figure 5a, separately for each ion species. The used bin size is 5 km. It is found that the depletion width is quite the same for all the analyzed ion species. The mean depletion width is overplotted by the black line. About 69% of PDEs have a depletion width less than 20 km. The density ratios (r_N) of analyzed ion species are shown in Figure 5b. A larger reduction in the ion number densities corresponds to lower values of r_N. The color lines show the results obtained for individual ion species, and the black line shows the mean ion density ratio. It can be seen that while the distributions of density ratios obtained for O^+, NO^+, and CO_2^+ are roughly the same, the density ratios obtained for the most abundant O_2^+ ion tend to be often much lower. A histogram of horizontal extents of PDEs (σ_G) is shown in Figure 5c. It can be seen that the ground trace of most events (about 84%) is between 200 and 800 km. For all identified depletion events, $\sigma_G > \sigma_Z$. We note, however, that larger σ_Z does not always correspond to larger σ_G and vice versa.

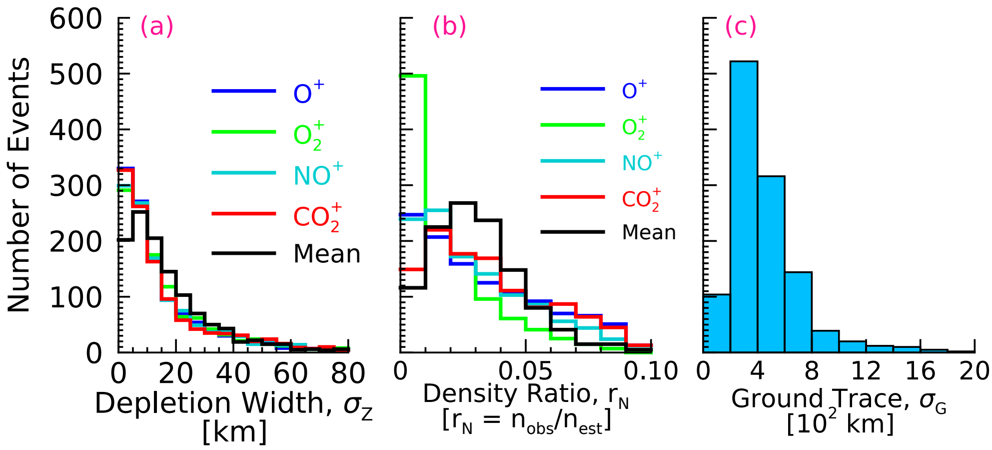

Figure 5. Histograms of parameters of plasma depletion events: (a) depletion thickness (σ_Z), (b) density ratios of ionospheric ions (r_N), and (c) the ground trace (σ_G).

4.2 Event Properties

Properties of PDEs as a function of solar zenith angle are shown in Figure 6. For ionospheric altitudes (above 120 km), the nightside ionosphere is illuminated up to SZA $\approx 105°$ and hence the actual nightside observations start at SZAs somewhat higher than 90° (Lillis et al., 2009; Dubinin et al., 2016). This threshold SZA can be clearly identified in all panels of Figure 6, as the number of identified PDEs increases significantly on the nightside.

The peak depletion altitudes depicted in Figure 6a exhibit a sudden change at the dayside/nightside boundary, they are almost exclusively above 200 km on the dayside. On the other hand, the peak depletion altitudes on the nightside are generally lower, below about 250 km for the vast majority of the events. Solar zenith angle dependences of average number density ratios and depletion thicknesses depicted in Figures 6b and 6c, respectively, do not reveal any clear trend. The ratio between the electron temperature measured at the peak depletion altitude and the expected electron temperature at the same height without the depletion event is termed the electron temperature ratio (r_T in Figure 6d). For most dayside PDEs (66%), the electron temperature ratio is between 1 and 2, and it does not seem to depend on SZA. The electron temperature ratios obtained for the nightside PDEs exhibit considerably larger scatter. They are still larger than 1 for most events (88% of events), but the values larger than 2 are rather common (46% of events).

Figure 7 shows the variations of peak depletion altitudes, magnetic field magnitudes at the times of the events, and electron temperature ratios with mean ion density ratio. The results obtained for the dayside and nightside events are plotted separately in the

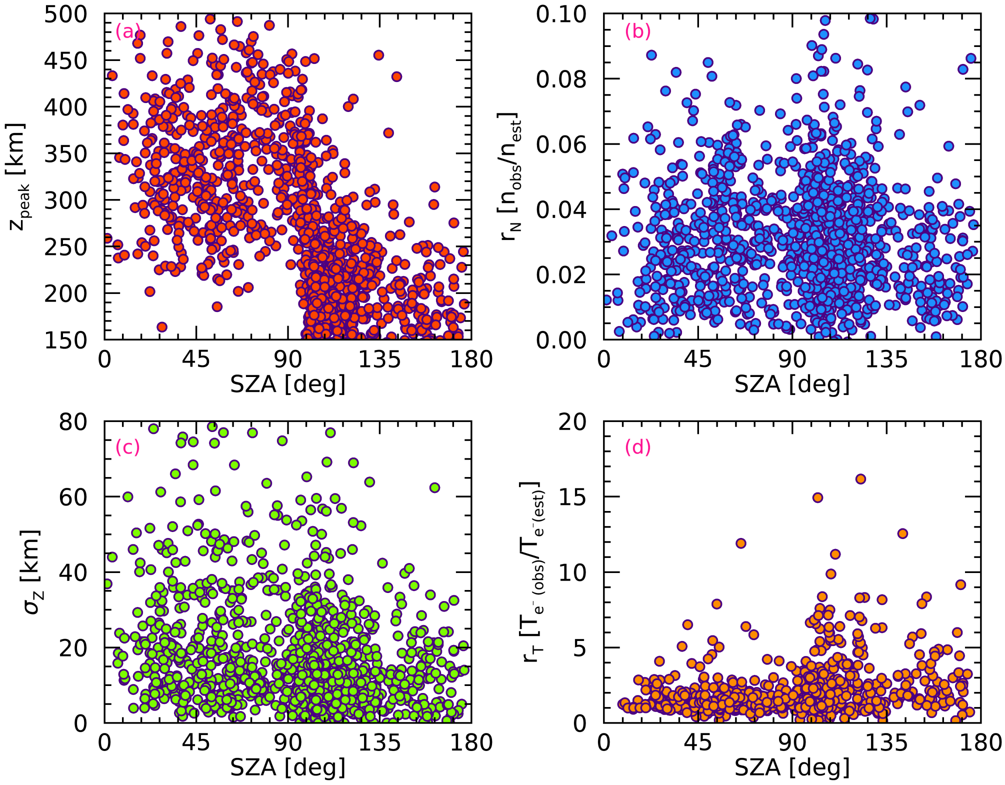

Figure 6. Parameters of individual identified plasma depletion events as a function of solar zenith angle: (a) peak depletion altitudes (z_{peak}), (b) ion density ratio (r_N), (c) depletion thickness (σ_Z), and (d) electron temperature ratio (r_T).

top and bottom panels, respectively. Typical values of dayside peak depletion altitudes depicted in Figure 7a are about 350 km, and they do not show any appreciable variations with the plasma depletion ratio. In contrast, nightside peak depletion altitudes are correlated with the density ratio; more significant density depletions occur preferentially at lower altitudes. We also note a considerable spread in z_{peak} at altitudes above about 250 km.

Figures 7c and 7d indicate that the magnetic field magnitude measured at the times of the events is essentially independent of the peak density ratio, both on the dayside and nightside. It is, however, noteworthy that the spread of magnetic field magnitudes observed during the nightside events is somewhat larger than during the dayside events. This is believed to be related to the crustal magnetic field influence and generally lower altitudes of nightside events. We also note that the magnetic field measured at the times of the events is typically almost horizontal both on the dayside and nightside. Although the scatter of electron temperature ratios is quite large, in particular on the nightside, Figures 7e and 7f indicate that they tend to be somewhat larger for more significant plasma depletions.

4.3 Geometry of the Events

The detection of PDEs at all ionospheric altitudes might suggest that the depletions are vertical column-like structures. Nevertheless, their observed horizontal extents are generally larger than vertical extents, suggesting a possibility of a horizontal layer

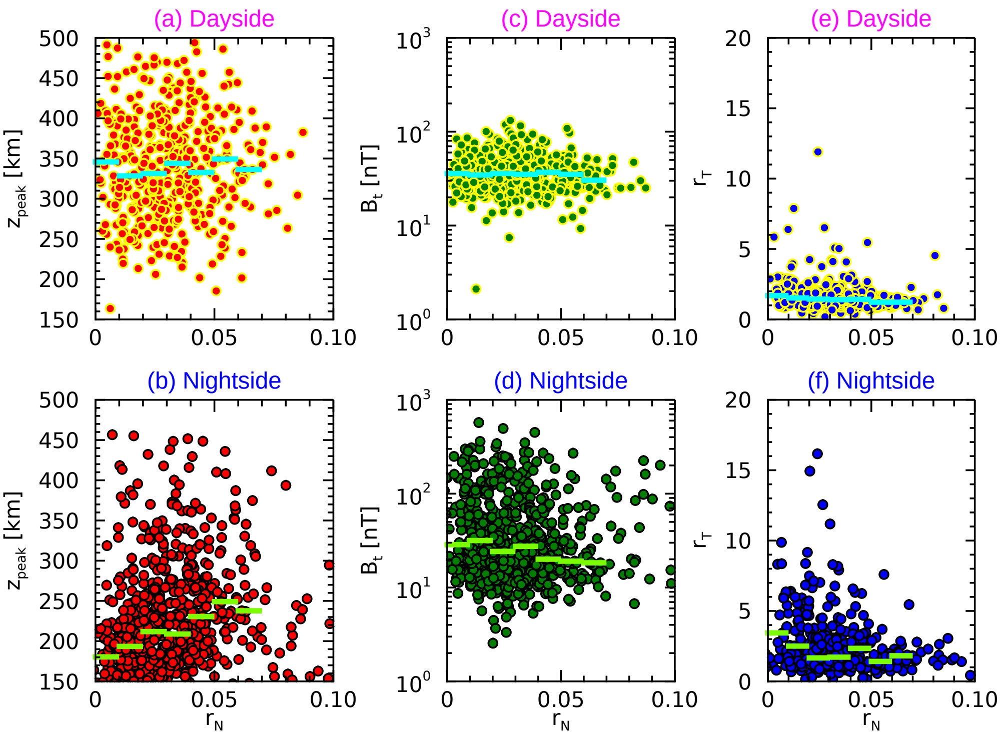

Figure 7. Parameters of individual identified PDEs as a function of ion density ratio. The results obtained for the dayside and nightside events are plotted in the top and bottom panels, respectively. (a)-(b) Peak depletion altitude (z_{peak}). (c)-(d) Magnetic field magnitude (B_t). (e)-(f) Electron temperature ratio (r_T). The overplotted horizontal lines mark the median values in individual intervals.

geometry. Given that only single-point measurements are available, it is difficult to distinguish these two scenarios experimentally. However, we attempt to use the fact that the orbital inclination ($\alpha = \arctan \nu_r/\nu_h$, where ν_r and ν_h are radial and horizontal components of the spacecraft velocity, respectively) varies from event to event to tackle this issue.

Schematic views of the two extreme geometry scenarios corresponding, to a horizontal layer depletion and a vertical column depletion are shown in Figures 8a and 8b respectively. Two different spacecraft trajectories, with two different inclination angles α, are shown in each figure. Assuming that the real PDEs would have a form of horizontal layers (Figure 8a), the observed vertical extents of the events would be independent of the orbital inclination ($\sigma_Z \approx const.$). Then, the observed horizontal extents would depend on the orbital inclination and were proportional to $1/\tan\alpha$. On the other hand, in a case of PDEs having a form of vertical columns (Figure 8b), the observed horizontal extents of the events would be independent of the orbital inclination ($\sigma_G \approx const.$), and the vertical extents would be proportional to $\tan\alpha$.

Plotting the horizontal and vertical extents of the events as a function of the orbital inclination should thus, in principle, allow distinguishing between the two geometry scenarios. This is done in Figures 9a and 9b, respectively. Each point corresponds to a single identified PDE, and the horizontal bars show the median values calculated in individual $\tan\alpha$ bins. It can be seen that the horizontal extent of the events σ_G is lower

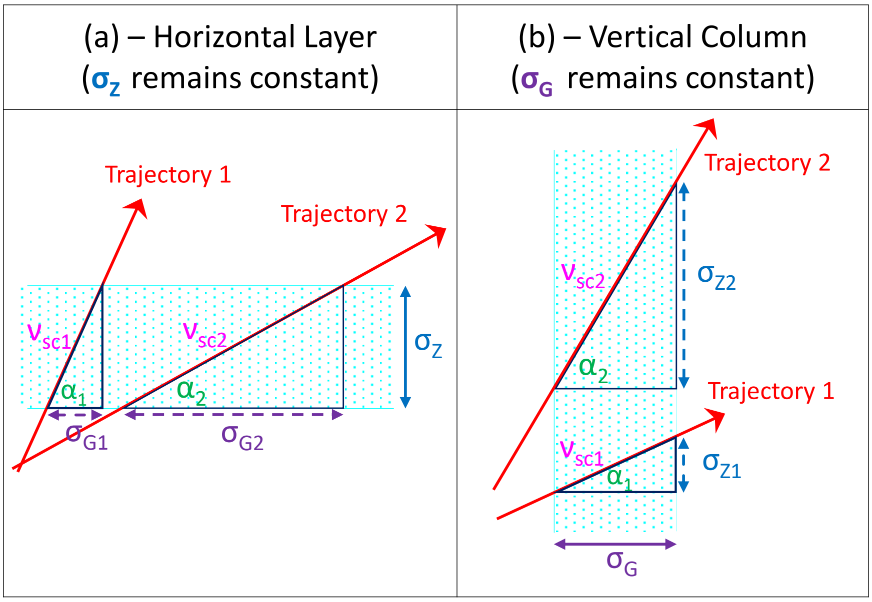

Figure 8. Schematic plots of two possible extreme scenarios of the event geometry. (a) Horizontal layer. (b) Vertical column. Two spacecraft trajectories with different orbital inclinations (α_1, α_2) are shown for each scenario, along with their respective ground (σ_G) and vertical (σ_Z) projections.

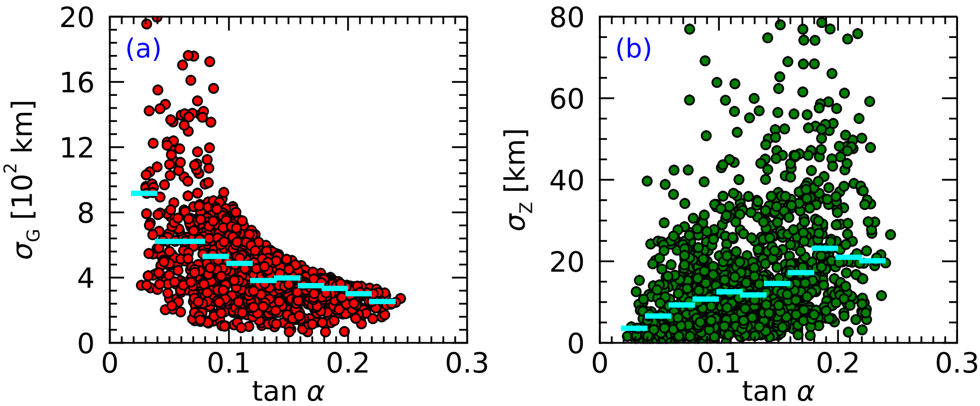

Figure 9. (a) Horizontal and (b) vertical extents of individual events as a function of tangent of orbital inclination. The overplotted horizontal lines mark the median values in individual intervals.

for larger orbital inclinations α, as would be expected for a horizontal layer geometry. However, at the same time, the vertical extent σ_Z increases with $\tan\alpha$, indicative of the vertical column geometry. This suggests that neither of the two extreme geometry scenarios is correct, with the actual event geometry possibly anywhere in between.

Thus, PDEs appear to be bubble-like ionospheric structures. Also, the arguably stronger dependence obtained for σ_G in Figure 9a than for σ_Z in Figure 9b may suggest that the real scenario is somewhat closer to the idealized case of a horizontal layer. This is in agreement with $\sigma_G > \sigma_Z$ observed in Figure 4.

5 Discussion

Large-scale electron density depressions (ionospheric holes) are known to exist in the nightside ionosphere of Venus at altitudes above about 200 km already for decades (Brace et al., 1980, 1982; Luhmann & Russell, 1992). While the exact mechanism driving the formation of these holes remains unclear, it is inferred that strong radial magnetic fields observed within the depression regions obstruct the neighboring plasma from replenishing these holes. Such ionospheric holes are thus strongly controlled by the magnetic pressure and the orientation of the draped interplanetary magnetic field (Collinson et al., 2014). By contrast, the Martian PDEs analyzed in our study occur both during the daytime and nighttime, and, on the nightside, they are mostly seen at altitudes below 200 km. The characteristics disparate from the Venusian ionospheric holes suggest that Martian PDEs are likely governed by different mechanisms. Moreover PDEs seems to be connected with remnant crustal magnetic field that is virtually absent at Venus.

Suprathermal electron depressions (referred to as plasma voids or electron holes) in the induced magnetosphere and ionosphere of Mars have been studied using MGS (Mitchell et al., 2001), Mars Express (Soobiah et al., 2006; Duru et al., 2011; Hall et al., 2016), and MAVEN (Steckiewicz et al., 2015, 2019). Plasma voids are proposed to be the direct consequence of the presence of rotating stronger crustal magnetic field regions (Mitchell et al., 2001). Considering that the energies of suprathermal electrons are much higher than the energies of thermal electrons and plasma we analyze in the present study, it might be difficult to draw any direct analogies. However, plasma voids are expected to occur below 200 km in the nightside ionosphere with closed crustal field lines (Xu et al., 2016, 2017). On the other hand, PDEs are found to often occur at higher altitudes on the dayside, with virtually undetectable magnetic field changes as compared to plasma voids. Hall et al. (2016) surveyed the electron holes in the induced magnetosphere of Mars in the energy range of 20–200 eV using the data from the MGS spacecraft, reporting most events in the altitude bin of 300 to 400 km. Although this altitudinal range is arguably comparable to the altitudes of dayside PDEs, the analyzed energies are still way larger than those of the thermal plasma. Duru et al. (2011) proposed that electron density depression events at the nightside may be due to the solar wind perturbations and plasma instabilities in the ionosphere. This can cause turbulence and possibly the streamers and/or plasma clouds at high altitudes.

According to Collinson et al. (2020), sudden reductions of the plasma densities may be explained by the displacement of plasma resulting from the collisions with neutral winds ($\vec{v}_{wind}$) and traversing across the magnetic field lines ($\vec{B}$), resulting in the electromagnetic forces ($\vec{v}_{wind} \times \vec{B}$). Their preliminary non-statistical study based on 34 events concluded that such a sporadic E-like structures occur primarily in the southern hemisphere with stronger crustal magnetic fields, near the magnetic field twist regions induced by the solar wind. Although the existence of sporadic E-like structures might explain small-scale increase/decrease in the electron density measurements (Withers et al., 2012), it does not seem to entirely account for the disparity in the dayside and nightside depletions, large-scale ground traces, and event occurrence also well above the Martian dynamo region. Keskinen (2018) argued that ionospheric plasma irregularities caused by the ion drifts (resulting from the neutral winds and magnetic field) are plausible only in the dynamo region at altitudes of about 125–250 km. In our case, almost all the dayside PDEs occur at altitudes well above.

The Martian dayside ionosphere is photochemically controlled below 200 km. In contrast, the plasma transport and diffusion dominate above these altitudes (Andrews, Edberg, et al., 2015). Additionally, the presence of strong crustal magnetic fields can affect both electron densities and electron temperatures at altitudes above 200 km (Dubinin et al., 2016). Nearly all identified daytime PDEs are in the plasma transport dominant region. In a transport-controlled region, increased electron temperatures can result in higher electron densities due to enhanced upward plasma flows (Flynn et al., 2017). Ergun et al. (2016) demonstrated that a higher electron temperature at these altitudes could develop strong enough ambipolar electric field to drift the major ions (O^+, O_2^+, CO_2^+), displacing them spatially and facilitating the ion escape. In addition, an increased plasma temperature at the times of an enhanced solar wind dynamic pressure can result in plasma clouds (Zhang et al., 2021), possibly removing the plasma from other regions. Nevertheless, the insignificant increase in electron temperature ratio eliminates the possibilities of plasma cloud formation and ion escape processes.

At altitudes below 300 km, the most abundant ion is O_2^+ (Benna et al., 2015). At higher altitudes, its density decreases exponentially with the scale height similarly to other species, except O^+ (Withers, 2009). Due to its significant abundance, O_2^+ ion has been envisaged to be the principal mechanism of oxygen loss in the Martian atmosphere up to 500 km. It has also been demonstrated that the loss due to a possible electric field-induced drift is more effective than the dissociative recombination loss of O_2^+ in comparison to other ions (Ergun et al., 2016). This suggests that the more profound depletions noticed in the O_2^+ ion densities could be due to additional loss processes through different channels apart from the PDE event formation mechanism itself.

Most nightside PDEs are seen below 250 km with large-scale ground traces and considerably increased electron temperatures. This may be due to the lack of a photochemically-dominant region, which is characteristic for the dayside ionosphere. In the dayside photochemical region, any plasma possibly removed in any way would be quickly replenished by photoionization, rendering the formation of depletion events very complicated and explaining possibly the lack of PDEs at low altitudes on the dayside. We note that the recombination coefficients are generally lower for higher electron temperatures (Schunk & Nagy, 2009; Dubinin et al., 2016), eliminating the possibility that the PDEs could be formed simply due to faster recombination. Since the nightside ionosphere of Mars is, at least close to the terminator, formed mainly due to plasma transported from the dayside (Němec et al., 2010; Lillis & Fang, 2015; Girazian et al., 2017), large number of PDEs detected close to the terminator can be perhaps attributed to the related ionospheric abundances. Additionally, the larger number of PDEs detected on the nightside than on the dayside may be perhaps related to their comparatively longer time of life, as the plasma sources on the nightside are extremely limited, and their eventual replenishing by the plasma may thus take much longer.

Brain et al. (2007) used MGS observations at ≈400 km to reveal the magnetic topology of Mars. The magnetic field lines are configured as draped (connected within the solar wind), open (connecting solar wind and the crustal magnetic field), and closed (connected within the crustal sources). Their study demonstrated that the northern hemisphere of Mars is dominated by draped/open field lines. In contrast, the magnetic field in the southern hemisphere is likely closed within the collisional atmosphere and sometimes connected to regions far from the strong crustal sources. Cusp-like configurations are noticed in areas with large radial magnetic components. The draped fields are almost horizontal at low altitudes close to the terminator regions (Dubinin et al., 2016; Weber et al., 2021). Below 200 km, the magnetic field lines are mostly closed and horizontal at nightside (Xu et al., 2016) which can weaken the electron-impact ionization process (Adams et al., 2018). At higher altitudes, draped and open field lines are observed more often above the weakly magnetized regions, which can connect to the nightside ionosphere even below the exobase (Weber et al., 2021). While the dayside PDEs occur at altitudes corresponding to draped and open field lines, most of nightside PDEs are identified within the closed field lines relating their origins to the crustal sources. This is consistent with the dominant horizontal magnetic component observed during the events.

The PDEs may be in a sense analogous to equatorial plasma bubbles encountered at Earth. These are sudden electron density depletions observed in the nightside equatorial ionosphere. Observations have confirmed the existence of plasma bubbles below the peak ionization region (about 200 km) and their eventual raising to altitudes up to about 1700 km (Oya et al., 1986; Otsuka et al., 2002, 2021). Rayleigh-Taylor instability is considered to be the most likely cause of the bubble formation at Earth (Kil, 2015; Oliveira et al., 2020). An uplifting plasma bubble can bifurcate due to an apparent shift in its central part. The stability of plasma bubbles depends on the electric field generated within (Otsuka et al., 2002).

6 Conclusions

We used MAVEN spacecraft data to identify and analyze plasma depletion events in the Martian ionosphere. These depletion events are distinguished by a sudden drop in ion number densities by at least an order of magnitude. At the same time, the electron temperature typically increases, especially during the nightside events. The magnetic field during the event observations is mostly horizontal, and it does not exhibit any significant variations.

Altogether, 1177 plasma depletion events are identified in the data measured from 18 October 2014 to 14 May 2021 using an automated identification algorithm. A statistical study of their occurrence reveals a strong solar zenith angle dependence, with more events occurring in the nightside ionosphere. Additionally, the nightside events occur predominantly in the southern hemisphere, suggesting their relation to the crustal magnetic fields. The dayside events appear mainly in the transport-dominant region at altitudes above about 200 km, while nightside events occur mostly at altitudes lower than 250 km.

It has been statistically found that the most abundant O_2^+ ion is depleted the most, while the depletions in other major ionospheric ions are somewhat smaller and roughly the same. The depletions likely have a form of bubble-like structures, with their ground traces being much larger than the altitudinal extents.

Although the depletion events may appear similar to the equatorial ionospheric plasma bubbles observed at Earth, it remains questionable whether they are formed by the same/similar mechanism. The exact formation mechanism of the depletion events thus remains unknown and will be addressed in the future.

Acknowledgments
F.N. acknowledges the support of the MSMT INTER-ACTION grant LTAUSA17070. The MAVEN mission is supported by NASA through the Mars Exploration Program. The MAVEN NGIMS (Level–02, Revision–01) data sets used in our study are publicly archived in NASA's Planetary Atmospheres Node (`https://atmos.nmsu.edu/PDS/data/PDS4/MAVEN/ngims_bundle/l2/`). The MAVEN LPW and MAG data products (Level–02, Insitu Key Parameters) used in this study are publicly archived in NASA's Planetary Plasma Interaction Node (`https://pds-ppi.igpp.ucla.edu/search/view/?f=yes&id=pds://PPI/maven.insitu.calibrated/data`).

References

Acuña, M. H., Connerney, J. E. P., Wasilewski, P., Lin, R. P., Anderson, K. A., Carlson, C. W., ... Ness, N. F. (1998). Magnetic Field and Plasma Observations at Mars: Initial Results of the Mars Global Surveyor Mission. *Science*, *279*(5357), 1676-1680. doi: 10.1126/science.279.5357.1676

Adams, D., Xu, S., Mitchell, D. L., Lillis, R. J., Fillingim, M., Andersson, L., ... Mazelle, C. (2018). Using Magnetic Topology to Probe the Sources of Mars'

Nightside Ionosphere. *Geophysical Research Letters*, *45*(22), 12,190-12,197. doi: 10.1029/2018GL080629

Andersson, L., Ergun, R. E., Delory, G. T., Eriksson, A., Westfall, J., Reed, H., ... Meyers, D. (2015). The Langmuir Probe and Waves (LPW) Instrument for MAVEN. *Space Science Reviews*, *195*(1-4), 173-198. doi: 10.1007/s11214-015-0194-3

Andrews, D. J., Andersson, L., Delory, G. T., Ergun, R. E., Eriksson, A. I., Fowler, C. M., ... Jakosky, B. M. (2015). Ionospheric plasma density variations observed at Mars by MAVEN/LPW. *Geophysical Research Letters*, *42*(21), 8862-8869. doi: 10.1002/2015GL065241

Andrews, D. J., Edberg, N. J. T., Eriksson, A. I., Gurnett, D. A., Morgan, D., Němec, F., & Opgenoorth, H. J. (2015). Control of the topside Martian ionosphere by crustal magnetic fields. *Journal of Geophysical Research: Space Physics*, *120*(4), 3042-3058. doi: 10.1002/2014JA020703

Benna, M., Mahaffy, P. R., Grebowsky, J. M., Fox, J. L., Yelle, R. V., & Jakosky, B. M. (2015). First measurements of composition and dynamics of the Martian ionosphere by MAVEN's Neutral Gas and Ion Mass Spectrometer. *Geophysical Research Letters*, *42*(21), 8958-8965. doi: 10.1002/2015GL066146

Bougher, Cravens, T. E., Grebowsky, J., & Luhmann, J. (2015). The Aeronomy of Mars: Characterization by MAVEN of the Upper Atmosphere Reservoir That Regulates Volatile Escape. *Space Science Reviews*, *195*(1-4), 423-456. doi: 10.1007/s11214-014-0053-7

Bougher, Jakosky, B., Halekas, J., Grebowsky, J., Luhmann, J., Mahaffy, P., ... Yelle, R. (2015). Early MAVEN Deep Dip campaign reveals thermosphere and ionosphere variability. *Science*, *350*(6261). doi: 10.1126/science.aad0459

Bougher, Pawlowski, D. J., Bell, J. M., Nelli, S. M., McDunn, T., Murphy, J., ... Ridley, A. J. (2015). Mars Global Ionosphere-Thermosphere Model: Solar cycle, seasonal, and diurnal variations of the Mars upper atmosphere. *Journal of Geophysical Research: Planets*, *120*(2), 311-342. doi: 10.1002/2014JE004715

Brace, L. H., Theis, R. F., Hoegy, W. R., Wolfe, J. H., Mihalov, J. D., Russell, C. T., ... Nagy, A. F. (1980). The dynamic behavior of the Venus ionosphere in response to solar wind interactions. *Journal of Geophysical Research: Space Physics*, *85*(A13), 7663-7678. doi: 10.1029/JA085iA13p07663

Brace, L. H., Theis, R. F., Mayr, H. G., Curtis, S. A., & Luhmann, J. G. (1982). Holes in the nightside ionosphere of Venus. *Journal of Geophysical Research: Space Physics*, *87*(A1), 199-211. doi: 10.1029/JA087iA01p00199

Brain, D. A., Lillis, R. J., Mitchell, D. L., Halekas, J. S., & Lin, R. P. (2007). Electron pitch angle distributions as indicators of magnetic field topology near Mars. *Journal of Geophysical Research: Space Physics*, *112*(A9). doi: 10.1029/2007JA012435

Cain, J. C., Ferguson, B. B., & Mozzoni, D. (2003). An n=90 internal potential function of the Martian crustal magnetic field. *Journal of Geophysical Research: Planets*, *108*(E2). doi: 10.1029/2000JE001487

Collinson, G., Fedorov, A., Futaana, Y., Masunaga, K., Hartle, R., Stenberg, G., ... Zhang, T. L. (2014). The extension of ionospheric holes into the tail of Venus. *Journal of Geophysical Research: Space Physics*, *119*(8), 6940-6953. doi: 10.1002/2014JA019851

Collinson, G., McFadden, J., Grebowsky, J., Mitchell, D., Lillis, R., Withers, P., ... Jakosky, B. (2020). Constantly forming sporadic E-like layers and rifts in the Martian ionosphere and their implications for Earth. *Nature Astronomy*, *4*, 1-6. doi: 10.1038/s41550-019-0984-8

Connerney, J., Espley, J., Lawton, P., Murphy, S., Odom, J., Oliversen, R., & Sheppard, D. (2015). The MAVEN Magnetic Field Investigation. *Space Science Reviews*, *195*(1-4), 257–291. doi: 10.1007/s11214-015-0169-4

Dubinin, E., Fraenz, M., Andrews, D., & Morgan, D. (2016). Martian Ionosphere observed by Mars Express: 1. Influence of the Crustal Magnetic Fields. *Planetary and Space Science*, *124*, 62 - 75. doi: 10.1016/j.pss.2016.02.004

Duru, F., Gurnett, D. A., Morgan, D. D., Modolo, R., Nagy, A. F., & Najib, D. (2008). Electron densities in the upper ionosphere of Mars from the excitation of electron plasma oscillations. *Journal of Geophysical Research: Space Physics*, *113*(A7). doi: 10.1029/2008JA013073

Duru, F., Gurnett, D. A., Morgan, D. D., Winningham, J. D., Frahm, R. A., & Nagy, A. F. (2011). Nightside ionosphere of Mars studied with local electron densities: A general overview and electron density depressions. *Journal of Geophysical Research: Space Physics*, *116*(A10). doi: 10.1029/2011JA016835

Ergun, R. E., Andersson, L. A., Fowler, C. M., Woodson, A. K., Weber, T. D., Delory, G. T., ... Jakosky, B. M. (2016). Enhanced O2+ loss at Mars due to an ambipolar electric field from electron heating. *Journal of Geophysical Research: Space Physics*, *121*(5), 4668-4678. doi: 10.1002/2016JA022349

Flynn, C. L., Vogt, M. F., Withers, P., Andersson, L., England, S., & Liu, G. (2017). MAVEN Observations of the Effects of Crustal Magnetic Fields on Electron Density and Temperature in the Martian Dayside Ionosphere. *Geophysical Research Letters*, *44*(21), 10,812-10,821. doi: 10.1002/2017GL075367

Fox, J. L., Brannon, J. F., & Porter, H. S. (1993). Upper limits to the nightside ionosphere of Mars. *Geophysical Research Letters*, *20*(13), 1339-1342. doi: 10.1029/93GL01349

Girazian, Z., Mahaffy, P., Lillis, R. J., Benna, M., Elrod, M., Fowler, C. M., & Mitchell, D. L. (2017). Ion Densities in the Nightside Ionosphere of Mars: Effects of Electron Impact Ionization. *Geophysical Research Letters*, *44*(22), 11,248-11,256. doi: 10.1002/2017GL075431

Hall, B. E. S., Lester, M., Nichols, J. D., Sánchez-Cano, B., Andrews, D. J., Opgenoorth, H. J., & Fränz, M. (2016). A survey of superthermal electron flux depressions, or "electron holes," within the illuminated Martian induced magnetosphere. *Journal of Geophysical Research: Space Physics*, *121*(5), 4835-4857. doi: 10.1002/2015JA021866

Hanson, W. B., Sanatani, S., & Zuccaro, D. R. (1977). The Martian Ionosphere as observed by the Viking Retarding Potential Analyzers. *Journal of Geophysical Research*, *82*(28), 4351-4363. doi: 10.1029/JS082i028p04351

Jakosky, B. M., Grebowsky, J. M., Luhmann, J. G., Connerney, J., Eparvier, F., Ergun, R., ... Yelle, R. (2015). MAVEN observations of the response of Mars to an Interplanetary Coronal Mass Ejection. *Science*, *350*(6261). doi: 10.1126/science.aad0210

Jakosky, B. M., Lin, R. P., Grebowsky, J. M., Luhmann, J. G., Mitchell, D. F., Beutelschies, G., ... Zurek, R. (2015). The Mars Atmosphere and Volatile Evolution (MAVEN) Mission. *Space Science Reviews*, *195*(1-4), 3-48. doi: 10.1007/s11214-015-0139-x

Keskinen, M. J. (2018). New Model for Ionospheric Irregularities at Mars. *Geophysical Research Letters*, *45*(5), 2177-2183. doi: 10.1002/2017GL076507

Kil, H. (2015). The Morphology of Equatorial Plasma Bubbles - a review. *Journal of Astronomy and Space Sciences*, *32*, 13-19. doi: 10.5140/JASS.2015.32.1.13

Krasnopolsky, V. A. (2002). Mars' Upper Atmosphere and Ionosphere at Low, Medium, and High Solar Activities: Implications for Evolution of Water. *Journal of Geophysical Research: Planets*, *107*(E12), 1–11. doi: 10.1029/2001JE001809

Lillis, R., Brain, D. A., Bougher, S. W., Leblanc, F., Luhmann, J. G., Jakosky, B. M., ... others (2015). Characterizing Atmospheric Escape from Mars today and through time, with MAVEN. *Space Science Reviews*, *195*(1-4), 357–422. doi: 10.1007/s11214-015-0165-8

Lillis, R., & Fang, X. (2015). Electron impact ionization in the Martian atmosphere: Interplay between scattering and crustal magnetic field effects. *Journal of Geo-*

physical Research: Planets, *120*(7), 1332-1345. doi: 10.1002/2015JE004841

Lillis, R., Fillingim, M. O., & Brain, D. A. (2011). Three-dimensional structure of the Martian nightside ionosphere: Predicted rates of impact ionization from Mars Global Surveyor magnetometer and electron reflectometer measurements of precipitating electrons. *Journal of Geophysical Research: Space Physics*, *116*(A12). doi: 10.1029/2011JA016982

Lillis, R., Fillingim, M. O., Peticolas, L. M., Brain, D. A., Lin, R. P., & Bougher, S. W. (2009). Nightside ionosphere of Mars: Modeling the effects of crustal magnetic fields and electron pitch angle distributions on electron impact ionization. *Journal of Geophysical Research: Planets*, *114*(E11). doi: 10.1029/2009JE003379

Luhmann, J. G., & Russell, D. S. (1992). Magnetic fields in Venus nightside ionospheric holes: Collected Pioneer Venus Orbiter magnetometer observations. *Journal of Geophysical Research: Planets*, *97*(E6), 10267-10282. doi: 10.1029/92JE00790

Mahaffy, P. R., Benna, M., Elrod, M., Yelle, R. V., Bougher, S. W., Stone, S. W., & Jakosky, B. M. (2015). Structure and Composition of the Neutral Upper Atmosphere of Mars from the MAVEN NGIMS Investigation. *Geophysical Research Letters*, *42*(21), 8951-8957. doi: 10.1002/2015GL065329

Mahaffy, P. R., Benna, M., King, T., Harpold, D. N., Arvey, R., Barciniak, M., ... others (2015). The Neutral Gas and Ion Mass Spectrometer on the Mars Atmosphere and Volatile Evolution Mission. *Space Science Reviews*, *195*(1-4), 49–73. doi: 10.1007/s11214-014-0091-1

McElroy, M. B., Kong, T. Y., Yung, Y. L., & Nier, A. O. (1976). Composition and Structure of the Martian Upper Atmosphere: Analysis of Results from Viking. *Science*, *194*(4271), 1295–1298. doi: 10.1126/science.194.4271.1295

Mendillo, M., Narvaez, C., Vogt, M. F., Mayyasi, M., Forbes, J., Galand, M., ... Andersson, L. (2017). Sources of Ionospheric Variability at Mars. *Journal of Geophysical Research: Space Physics*, *122*(9), 9670-9684. doi: 10.1002/2017JA024366

Mitchell, D. L., Lin, R. P., Mazelle, C., Rème, H., Cloutier, P. A., Connerney, J. E. P., ... Ness, N. F. (2001). Probing Mars' crustal magnetic field and ionosphere with the MGS Electron Reflectometer. *Journal of Geophysical Research: Planets*, *106*(E10), 23419-23427. doi: 10.1029/2000JE001435

Nier, A. O., & McElroy, M. B. (1976). Structure of the Neutral Upper Atmosphere of Mars: Results from Viking 1 and Viking 2. *Science*, *194*(4271), 1298–1300. doi: 10.1126/science.194.4271.1298

Němec, F., Morgan, D. D., Gurnett, D. A., & Brain, D. A. (2011). Areas of enhanced ionization in the deep nightside ionosphere of Mars. *Journal of Geophysical Research: Planets*, *116*(E6). doi: 10.1029/2011JE003804

Němec, F., Morgan, D. D., Gurnett, D. A., & Duru, F. (2010). Nightside ionosphere of Mars: Radar soundings by the Mars Express spacecraft. *Journal of Geophysical Research: Planets*, *115*(E12). doi: 10.1029/2010JE003663

Němec, F., Morgan, D. D., Gurnett, D. A., Duru, F., & Truhlík, V. (2011). Dayside ionosphere of Mars: Empirical model based on data from the MARSIS instrument. *Journal of Geophysical Research: Planets*, *116*(E7). doi: 10.1029/2010JE003789

Oliveira, C. B. A. d., Espejo, T. M. S., Moraes, A., Costa, E., Sousasantos, J., Lourenço, L. F. D., & Abdu, M. A. (2020). Analysis of Plasma Bubble Signatures in Total Electron Content Maps of the Low-Latitude Ionosphere: A Simplified Methodology. *Surveys in Geophysics*, *41*(4), 897-931. doi: 10.1007/s10712-020-09584-7

Otsuka, Y., Shinbori, A., Sori, T., Tsugawa, T., Nishioka, M., & Huba, J. D. (2021). Plasma depletions lasting into daytime during the recovery phase of a geomagnetic storm in May 2017: Analysis and simulation of GPS total electron content observations. *Earth and Planetary Physics*, *5*, 427. doi: 10.26464/epp2021046

Otsuka, Y., Shiokawa, K., Ogawa, T., & Wilkinson, P. (2002). Geomagnetic conjugate observations of equatorial airglow depletions. *Geophysical Research Letters*, *29*(15), 43-1-43-4. doi: 10.1029/2002GL015347

Owen, T., & Biemann, K. (1976). Composition of the Atmosphere at the Surface of Mars: Detection of Argon-36 and Preliminary Analysis. *Science*, *193*(4255), 801–803. doi: 10.1126/science.193.4255.801

Oya, H., Takahashi, T., & Watanabe, S. (1986). Observation of Low Latitude Ionosphere by the Impedance Probe on Board the Hinotori Satellite. *Journal of Geomagnetism and Geoelectricity*, *38*(2), 111-123. doi: 10.5636/jgg.38.111

Picardi, G., Plaut, J. J., Biccari, D., Bombaci, O., Calabrese, D., Cartacci, M., . . . Zampolini, E. (2005). Radar Soundings of the Subsurface of Mars. *Science*, *310*(5756), 1925-1928. doi: 10.1126/science.1122165

Schunk, R., & Nagy, A. (2009). *Ionospheres: Physics, Plasma Physics, and Chemistry* (2nd ed.). Cambridge University Press. doi: 10.1017/CBO9780511635342

Sánchez-Cano, B., Lester, M., Witasse, O., Milan, S. E., Hall, B. E. S., Cartacci, M., . . . Pätzold, M. (2016). Solar cycle variations in the ionosphere of Mars as seen by multiple Mars Express data sets. *Journal of Geophysical Research: Space Physics*, *121*(3), 2547-2568. doi: 10.1002/2015JA022281

Soffen, G. A. (1976). Scientific Results of the Viking Missions. *Science*, *194*(4271), 1274–1276. doi: 10.1126/science.194.4271.1274

Soobiah, Y., Coates, A., Linder, D., Kataria, D., Winningham, J., Frahm, R., . . . Dierker, C. (2006). Observations of magnetic anomaly signatures in Mars Express ASPERA-3 ELS data. *Icarus*, *182*, 396-405. doi: 10.1016/j.icarus.2005.10.034

Steckiewicz, M., Garnier, P., André, N., Mitchell, D. L., Andersson, L., Penou, E., . . . Jakosky, B. M. (2017). Comparative study of the Martian suprathermal electron depletions based on Mars Global Surveyor, Mars Express, and Mars Atmosphere and Volatile EvolutioN mission observations. *Journal of Geophysical Research: Space Physics*, *122*(1), 857-873. doi: 10.1002/2016JA023205

Steckiewicz, M., Garnier, P., Lillis, R., Toublanc, D., Leblanc, F., Mitchell, D. L., . . . Mazelle, C. (2019). Dawn/Dusk Asymmetry of the Martian UltraViolet Terminator Observed Through Suprathermal Electron Depletions. *Journal of Geophysical Research: Space Physics*, *124*(8), 7283-7300. doi: 10.1029/2018JA026336

Steckiewicz, M., Mazelle, C., Garnier, P., André, N., Penou, E., Beth, A., . . . Jakosky, B. M. (2015). Altitude dependence of nightside Martian suprathermal electron depletions as revealed by MAVEN observations. *Geophysical Research Letters*, *42*(21), 8877-8884. doi: 10.1002/2015GL065257

Weber, T., Brain, D., Xu, S., Mitchell, D., Espley, J., Mazelle, C., . . . Jakosky, B. (2021). Martian Crustal Field Influence on O+ and O2+ Escape as Measured by MAVEN. *Journal of Geophysical Research: Space Physics*, *126*(8), e2021JA029234. doi: 10.1029/2021JA029234

Withers, P. (2009). A review of observed variability in the dayside ionosphere of Mars. *Advances in Space Research*, *44*(3), 277-307. doi: 10.1016/j.asr.2009.04.027

Withers, P., Fallows, K., Girazian, Z., Matta, M., Häusler, B., Hinson, D., . . . Witasse, O. (2012). A clear view of the multifaceted dayside ionosphere of Mars. *Geophysical Research Letters*, *39*(18). doi: 10.1029/2012GL053193

Xu, S., Mitchell, D., Liemohn, M., Dong, C., Bougher, S., Fillingim, M., . . . Jakosky, B. (2016). Deep nightside photoelectron observations by MAVEN SWEA: Implications for Martian northern hemispheric magnetic topology and nightside ionosphere source. *Geophysical Research Letters*, *43*(17), 8876-8884. doi:

10.1002/2016GL070527

Xu, S., Mitchell, D., Liemohn, M., Fang, X., Ma, Y., Luhmann, J., … Jakosky, B. (2017). Martian low-altitude magnetic topology deduced from MAVEN/SWEA observations. *Journal of Geophysical Research: Space Physics*, *122*(2), 1831-1852. doi: 10.1002/2016JA023467

Zhang, C., Rong, Z., Nilsson, H., Klinger, L., Xu, S., Futaana, Y., … Cui, J. (2021). MAVEN Observations of Periodic Low-altitude Plasma Clouds at Mars. *The Astrophysical Journal Letters*, *922*, L33. doi: 10.3847/2041-8213/ac3a7d